Effects of shape distortions and imperfections on mode frequencies and collective linewidths in nanomagnets

H. T. Nembach,[1] Justin M. Shaw,[1] T. J. Silva,[1] W. L. Johnson,[2] S. A. Kim,[2] R. D. McMichael,[3] and P. Kabos[1]

[1]*Electromagnetics Division, National Institute of Standards and Technology, Boulder, Colorado 80305, USA*

[2]*Materials Reliability Division, National Institute of Standards and Technology, Boulder, Colorado 80305, USA*

[3]*Center for Nanoscale Science and Technology, National Institute of Standards and Technology, Gaithersburg, Maryland 20899, USA*

(Received 5 November 2010; revised manuscript received 9 February 2011; published 28 March 2011)

Brillouin light scattering shows that shape distortions in $Ni_{80}Fe_{20}$ nanomagnets can have a dramatic effect on the measured collective linewidth of certain spin-wave modes. The intentional introduction of quantifiable asymmetric egglike shape distortion to an ideal elliptical structure lifts the degeneracy of end modes with concentrated amplitude at the nanomagnet edges. In contrast, modes with concentrated amplitude at the interior are significantly less affected by the distortion. The splitting of end modes by asymmetric distortions explains the large inhomogeneous linewidth broadening in end modes found in large ensembles of nanomagnets that contain a relatively small statistical variation in the degree of distortion.

I. INTRODUCTION

Magnetization dynamics and damping mechanisms in nanomagnets are of special interest due to emerging applications in spin-torque devices and high-density magnetic recording media. The strength of the damping in nanomagnets is a critical parameter because it strongly influences the magnitude of the critical current for the onset of spin-torque effects[1,2] and may determine the feasibility of microwave assisted magnetic recording (MAMR).[3] There remain open questions as to how the damping parameter α changes when moving from extended thin films to patterned nanomagnets. For example, there are numerous conflicting reports concluding whether or not the damping is enhanced through the nanopatterning process.[4–8] Separating intrinsic and extrinsic sources of linewidth in nanomagnetics is a natural first step to understanding such behavior.

We previously studied the ferromagnetic resonance (FMR) in $Ni_{80}Fe_{20}$ nanomagnets for a range of diameters and thicknesses by use of the frequency-resolved magneto-optical Kerr effect (FR-MOKE). Two different spin-wave modes were identified in 200-nm-diameter ellipsoidal nanomagnets.[8] Micromagnetic simulations showed that the higher frequency mode is broadly distributed throughout the central volume of the nanomagnet, and the lower frequency mode is sharply localized at the ends of the nanomagnet (hereafter referred to as the *center mode* and the *end mode*, respectively). Similar mode profiles were also reported in different systems.[9,10] The end mode in Ref. 8 shows significant additional linewidth broadening compared to an unpatterned thin film. A variation in the size of the individual ellipsoidal nanomagnets would yield an additional linewidth broadening, but size variations alone were not sufficient to explain the enhanced end-mode linewidth.[8] Since that study was performed on a large ensemble of nanomagnets, we make the distinction between the linewidth of an individual nanomagnet and the *collective* linewidth of the ensemble. In the latter case, a statistical variation of resonance properties from nanostructure to nanostructure can give rise to an increased collective linewidth when the array is measured as a whole. This effect on the collective linewidth is convoluted with any intrinsic sources of linewidth found in an individual nanomagnet.

In that same work, micromagnetic simulations suggested that small stochastic distortions from the ideal ellipsoid shape of the individual nanomagnets would result in a distribution of resonance frequencies in a lithographically patterned array.[8] Such a mode frequency distribution was predicted to broaden the measured collective FMR linewidth. In order to test this hypothesis, we prepared arrays of $Ni_{80}Fe_{20}$ nanomagnets with intentional and quantifiable distortions from an ideal elliptical shape. The spin-wave frequencies were measured by Brillouin light scattering spectroscopy (BLS) as a function of the in-plane applied magnetic-field angle and compared to micromagnetic simulations for similarly distorted nanomagnets. We will show that such shape distortions can explain the significant increase in collective end-mode linewidth found in ensembles of nanomagnets reported in Ref. 8.

II. EXPERIMENT

The arrays of nanomagnets were fabricated using electron-beam lithography (EBL). Thin-film layers of 3 nm Ta/10 nm $Ni_{80}Fe_{20}$/5 nm Si_3N_4 were dc-magnetron sputtered onto a sapphire substrate before a 15-nm diamondlike carbon (DLC) layer was deposited via ion-beam deposition. EBL was then used to expose a polymethyl methacrylate (PMMA) layer, followed by the liftoff of a 5-nm, ion-beam deposited Cr layer. The pattern was transferred to the DLC layer via an O_2 plasma etch before the Cr was removed with a wet etch. The final pattern transfer to the $Ni_{80}Fe_{20}$ layer was accomplished by a 300-eV Ar ion mill. Finally, the remaining DLC was removed by a second O_2 plasma etch.

The egglike ("eggcentric") distortion introduced into the nominally 200-nm elliptical structures is defined by

$$\frac{x^2}{A^2} + \frac{y^2}{B^2 \exp\left(\frac{-|c|x}{A}\right)} = 1,\qquad(1)$$

where A and B define the ellipticity and c defines the amount of eggcentricity. When $c = 0$, the equation for an ellipse is

(a)

Ellipse

200nm

(b)

Egg1

200nm

(c)

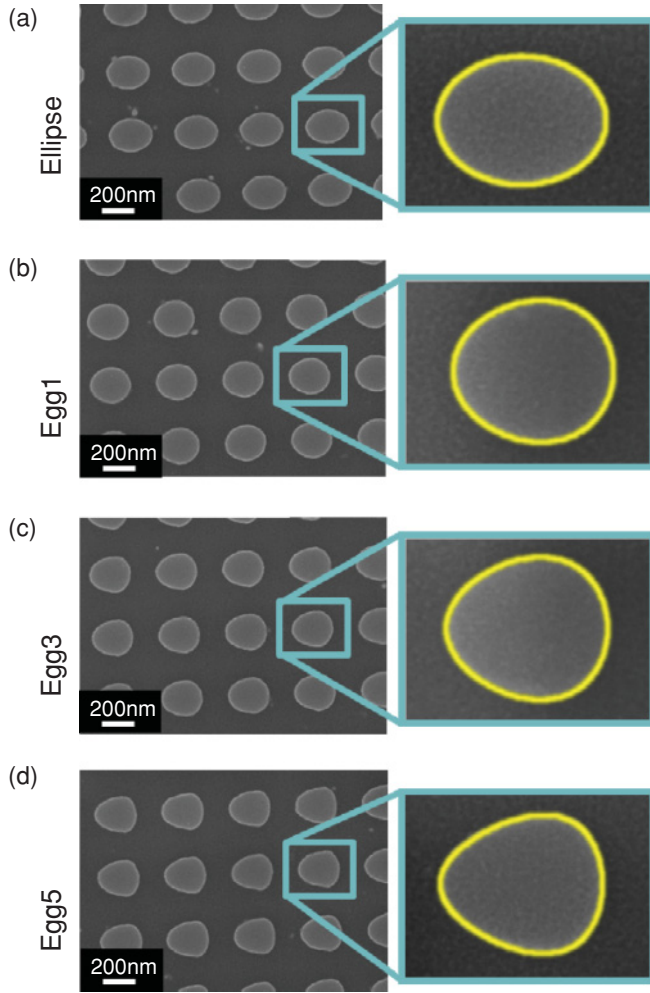Egg3

200nm

(d)

Egg5

200nm

FIG. 1. (Color online) SEM images of the four different arrays with nanomagnets exhibiting different amounts of eggcentricity. The yellow line along the contour of the individual ellipse is a fit of Eq. (1) to the actual shape of the nanomagnets. The resultant fitting parameter values for the long axis A, the short axis B, and the eggcentricity c are given in Table I.

recovered. Since the actual shape after fabrication might differ from the ideal shape, we fit the above equation to images taken with a scanning electron microscope (SEM). The images of the elliptical structures and structures with three different values for c are shown in Fig. 1. The closest fits to Eq. (1) are overlaid in the figures and the corresponding values of A, B, and c are given in Table I. The samples are hereafter referred to as ellipse, egg1, egg3, and egg5 with increasing values of c.

We measured the spin-wave frequencies in these arrays with BLS.[11] The wavelength of the laser beam was $\lambda = 532$ nm and the angle of incidence was $45°$. Spin-wave spectra were taken for different angles φ of the applied in-plane magnetic field of $\mu_0 H = 0.1$ T with respect to the long axis of the ellipses. A sketch of the scattering geometry is shown in Fig. 2 with the x axis in the plane of incidence and the z axis perpendicular to the sample surface.

BLS measures thermally excited spin waves, and therefore requires no external excitation of the spin-wave modes.
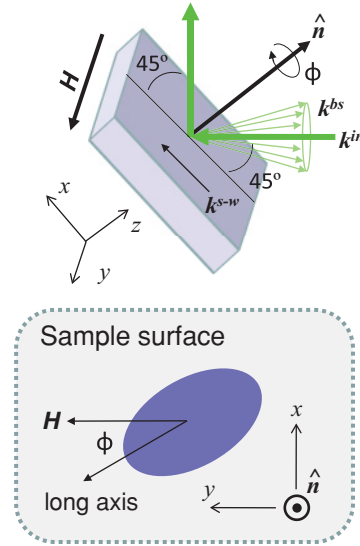
FIG. 2. (Color online) Sketch of the BLS measurement geometry, where ϕ is the in-plane angle between the long axis of the ellipsoids and the applied magnetic field H. The incident laser beam is scattered by a spin wave with in-plane wave vector k^{s-w}. The wave vector of the incident and backscattered beams are k^{in} and k^{bs}, respectively. The vector $\boldsymbol{n}$ denotes the surface normal.

The leading term of the scattering cross section for the backscattering geometry in the BLS experiment is given by

$$\sigma(k) \propto \left| \iint \delta m_z(x,y) \cdot e^{ikx} dx dy \right|^2, \qquad (2)$$

where the integral extends over the part of the array that is illuminted by the laser spot.[12,13] $\delta m_z(x,y)$ is the dynamic out-of-plane component of the magnetization, and k is the in-plane component along the x axis of the scattering wave vector with $k = 4\pi/\lambda \cdot \sin(45°) = 16.7$ rad/μm in our measurements. The scattering cross section for each spin-wave mode is essentially proportional to its Fourier transform with respect to the scattering wave vector. Therefore spin-wave modes, which are antisymmetric with respect to the y coordinate (perpendicular to the plane of incidence), cannot be detected by BLS. A more detailed discussion of the scattering cross section can be found in Refs. 14 and 15.

We carried out micromagnetic simulations using the object-oriented micromagnetic framework (OOMMF) package[16] to predict the localization of the various spin-wave modes measured by BLS. Spin-wave modes were excited deterministically in the simulations by field pulses that have both a spatially uniform component and a spatial gradient

TABLE I. Results of a fit with Eq. (1) to the actual contour of the nanomagnets; see Fig. 1.

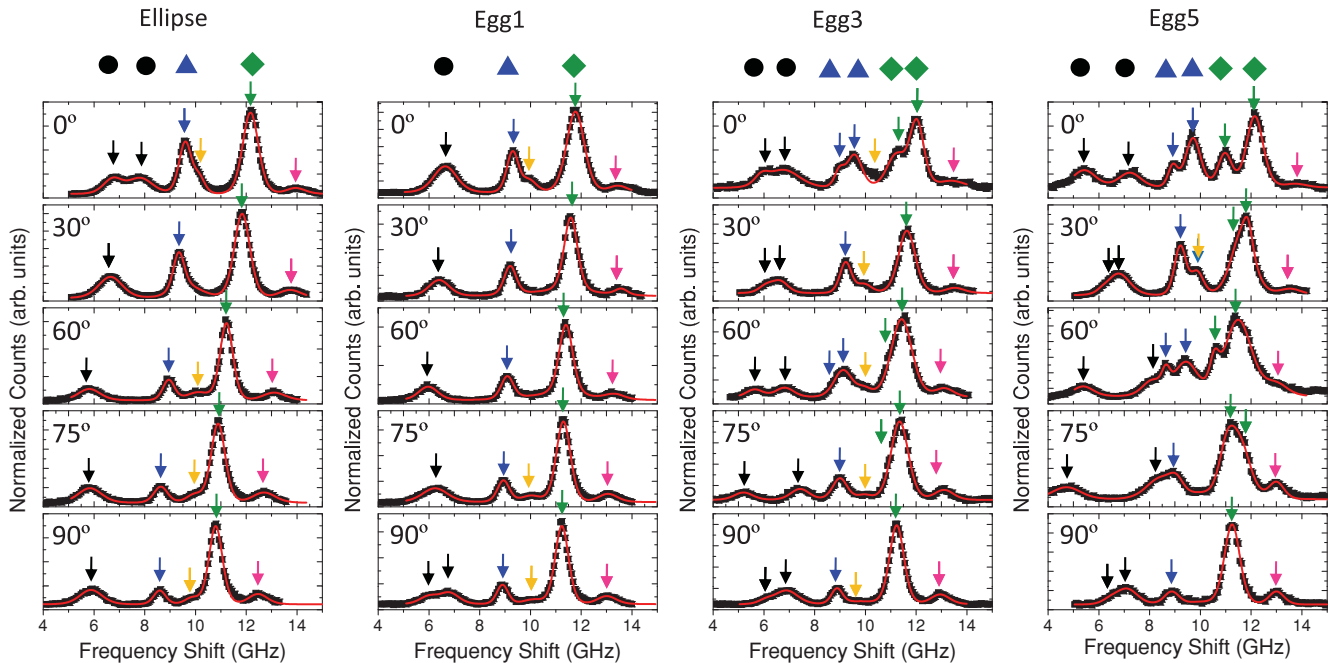| Sample	A (nm)	B (nm)	c
Ellipse	274	212	0
Egg1	256	226	0.2
Egg3	255	226	0.35
Egg5	256	210	0.6

FIG. 3. (Color online) Dependence of nanomagnet spin-wave spectra on c for different directions of the applied magnetic field. The red line is a fit to the data by use of a superposition of several Lorentians raised to the sixth power, corresponding to the number of peaks measured in the respective spectra. The colored arrows together with the symbols denote the different spin-wave modes.

component. Both the pulse field direction and the pulse field gradient are perpendicular to the applied field. The pulse field gradient is required to excite antisymmetric modes with nodal lines running roughly parallel to the applied field. The relative magnitude of the constant and gradient field pulses was adjusted until the symmetric and antisymmetric modes had comparable amplitudes. Simulations were performed at varying in-plane field angles.

III. RESULTS AND DISCUSSION

Figure 3 shows several BLS spectra for arrays with different eggcentricities at five different angles of the applied field φ with respect to the long axis of the ellipse. The peaks in the spectra were simultaneously fit to a model function that consisted of sum of Lorentzians, each raised to the sixth power. The model function is the transmission function of the (3+3)-pass tandem Fabry-Perot interferometer convolved with the Lorentzian line shape of the spin-wave mode.[17] The red line in Fig. 3 is a fit to the data with a superposition of modeled peak functions that correspond to the number of well-defined peaks in the respective spectra. The colored arrows mark the peaks of the different spin-wave modes. The number of spin-wave peaks generally appears to increase with increasing eggcentricity. Some of the spin-wave modes split into two nondegenerate frequencies for particular values of φ. This behavior is more pronounced for the samples with greater eggcentricity. The angular dependence of the strongest peaks in the BLS spectra is shown in Fig. 4. Three prominent and intense spin-wave modes can be identified for the four samples. These modes are denoted by black circles, blue triangles, and green diamonds. All three modes have a minimum frequency at $\varphi = 90°$ for the ellipse. When the external magnetic field is along the short axis

of the ellipse the demagnetizing field is at its maximum leading to a lower internal field and thus lower mode frequencies. Only the lowest frequency mode splits for certain angles of the applied field for the ellipse and egg1. However, for the egg3 sample with $c = 0.35$, the highest frequency mode also splits. In addition, the lowest frequency mode splits and recombines at multiple azimuthal angles. Finally, for the egg5 sample with $c = 0.6$, all three modes split and recombine. The average frequency for the three main modes remains insensitive to eggcentricity, but the frequency separation of the splitting for the two lowest frequency modes has increased from about 1 GHz to more than 4 GHz between $c = 0$ and $c = 0.65$.

The results of micromagnetic simulations are shown in Fig. 5. The left panel shows the different modes and their spatial amplitude distribution for the ellipse, i.e., $c = 0$. The right panel shows the same for $c = 0.65$, corresponding to sample egg5. The four rows show the results for different values of φ, increasing from top to bottom. In each row the ground state of the magnetization is shown for the ellipse and the egg5 sample. The three predominate modes found in the experimental data are also identified in the simulations. From the spatial amplitude plots (insets in Fig. 5), we conclude that the lowest frequency mode is localized at the ends of the ellipse, and the next higher frequency mode is concentrated in the center of the ellipse. These two modes are consistent with the respective *end mode* and *center mode* identified in Ref. 8. However, the highest frequency mode has its nodal line along the field axis.

The frequencies of the spin-wave modes are shown in Fig. 6 as a function of φ. The width of the lines in Fig. 6 conveys the mode amplitude. We note that simulations are not expected to exactly reproduce the spectral amplitudes of thermal modes, nor have we included the BLS scattering cross
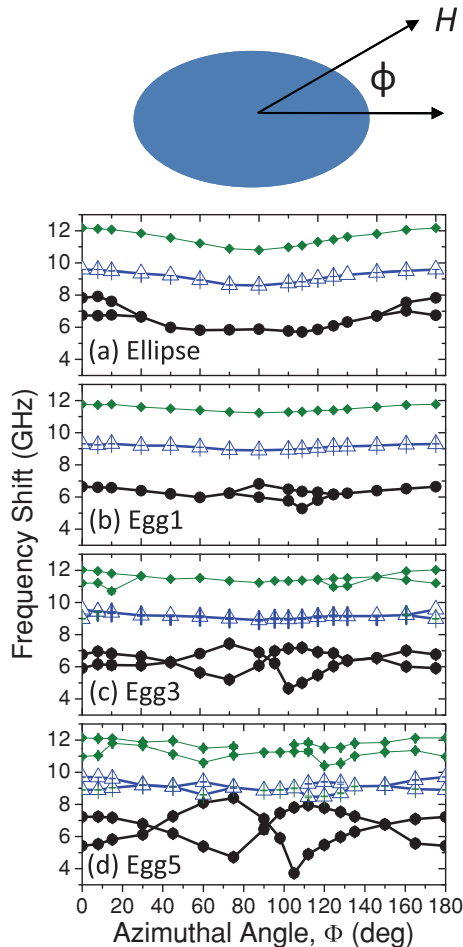
FIG. 4. (Color online) Angular dependence of the strongest spin-wave modes measured with BLS for samples of varying eggcentricity. Three major spin-wave modes can be identified. The lowest frequency mode is denoted with filled black circles. This mode is identified as the edge mode. The next highest frequency mode is indicated with blue triangles. It is identified as the center mode. The highest frequency mode is denoted with filled green diamonds. For certain angles of the applied field these modes split into two modes.

sections in our simulations. However, the relative amplitudes in the simulations provide a rough trend and are in qualitative agreement with the measurements.

The dependence of mode frequency on φ agrees very well with the data. However, simulations and experiment differ on the splitting of the end mode for the ellipse sample with $c = 0$ observed in the BLS spectra; such splitting does not occur in the simulations. We speculate that either the additional mode does not couple to the pulse field in the simulations due to its symmetry, or that end-mode splitting is manifested in the data because there is sufficient unintended shape distortion in the actual patterned arrays relative to the nominally ideal ellipse. However, a collective dynamical behavior of the nanomagnets is highly unlikely to be the origin of this mode splitting. It was shown that the interaction of the end modes within a single 160 nm × 350 nm × 5 nm of isotropic Permalloy is negligible.[18] Also, the coupling strength is approximately equal for all the arrays investigated in this study. Since the end mode splitting at $\varphi = 0°$ is not observed in all of the arrays,

we can conclude that it is a result of the specific shape of the nanostructures within a particular array.

The end modes show the strongest dependence on c for both the BLS spectra and the simulations. We understand that this dependence stems from the localization of the mode at the ends of the ellipse: The mode frequency depends on the magnitude of local internal demagnetizing field. As such, a change of the curvature at the ends of the ellipse alters the local demagnetizing field and thereby changes the local mode frequency. The right panel in Fig. 5 with the simulation results for $c = 0.65$ demonstrates the large influence of edge curvature on frequency. For the $\varphi = 0°$ simulation, the frequencies are nondegenerate for the two end modes (i.e., the black spectral peaks). However, their frequencies become degenerate for the $\varphi = 90°$ simulation. For $\varphi = 90°$, the two end modes are located at positions with identical curvature. On the other hand, the center mode (i.e., the blue spectral peak) is less sensitive to changes of the curvature of the nanomagnet edges. It exhibits smaller frequency splitting for certain directions of the external field even for the highly distorted egg5 sample. The highest frequency mode exhibits splitting between that of the end mode and center mode. This is consistent with the fact that its amplitude is concentrated near the edge region, but not to the same extent as the low-frequency end mode.

The different sensitivities of these various modes to distortion of shape can explain previous FR-MOKE measurements of end- and center-mode linewidths in arrays of nominally elliptical nanomagnets. (See Ref. 8 for details about the experiment and the results.) This previously measured sample was an array of $Ni_{80}Fe_{20}$ 220 nm × 202 nm ellipses with a thickness of 5 nm. The inset in Fig. 7 shows the field dependence of the resonance frequency f_0 for the end mode (blue triangles) and the center mode (black circles) measured by FR-MOKE. The sample was excited by a spatially uniform cw microwave field oriented perpendicular to a static field applied parallel to the long axes of the ellipses. The spatially uniform microwave field does not excite modes that are antisymmetric with respect to a plane parallel to the external magnetic field. Thus the third BLS mode (the green spectral peak in Fig. 5) is not present in the FR-MOKE spectra, leaving only the end mode (black) and the center mode (blue) as experimentally accessible in the previous FR-MOKE study.[8]

The 1 GHz splitting of the end mode found in the BLS spectra of the $c = 0$ ellipses for $\phi < 30°$ and $\phi > 150°$ was not observed in the FR-MOKE experiment. We speculate that either the shape distortions in the nominally perfect ellipses used in Ref. 8 were sufficiently small that the mode splitting was not resolvable, or that the second mode did not couple to the rf field due to its symmetry and was therefore not excited.

The full width at half maximum (FWHM) linewidths of the end and center modes versus frequency measured by FR-MOKE are shown in Fig. 7 (see Ref. 8). The frequency dependence of the linewidth was initially fitted with the phenomenological equation:[19]

$$\Delta H(f) = \Delta H_0 + \frac{4\pi\alpha}{|\gamma|\mu_0} \cdot f, \qquad (3)$$

where γ is the gyromagnetic ratio, μ_0 is the vacuum permeability, f is the microwave frequency, and α the intrinsic damping
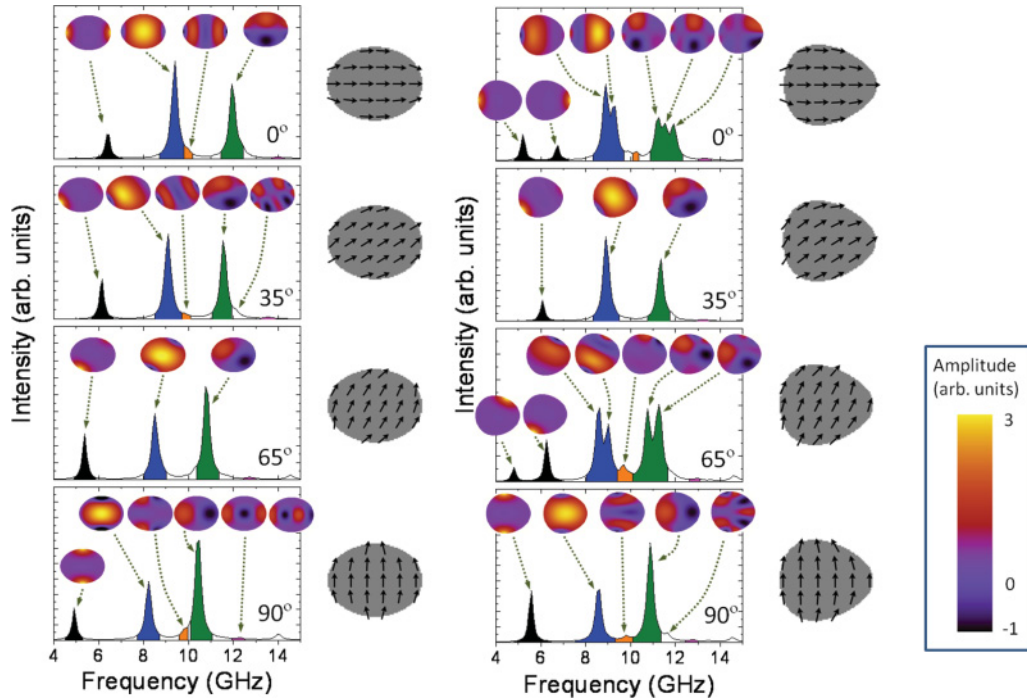
FIG. 5. (Color online) Micromagnetic simulation results. The left panel shows the frequency and the spatial distributions for the spin-wave modes of the ellipse and the right panel for sample egg5 with the largest value of c. The rows show the simulations for the different angles between the long axis of the ellipse and the applied magnetic field. The static ground state of the magnetization of the ellipse and the egg5 sample are shown in each row next to the results of the frequency distribution.

parameter. A nonzero intercept ΔH_0 is commonly attributed to sample inhomogeneity such as locally varying magnetic anisotropy. The linewidth of the end mode (black squares) is considerably broader than that for the center mode (red circles). A fit of the data with Eq. (3) (not shown) yields values of $\alpha = 0.01 \pm 0.001$ and $\mu_0 \Delta H_0 = 1.0 \pm 0.5$ mT for the center mode and $\alpha = 0.013 \pm 0.003$, $\mu_0 \Delta H_0 = 6.4 \pm 1.0$ mT for the end mode.[8] The fitted inhomogenous linewidth broadening for the end mode is significantly larger than for the center mode. One contribution to the inhomogeneous broadening was attributed to the size variation among the nanomagnets; the resonance field for each nanomagnet varies due to this size variation, which leads to increased measured linewidth. If one assumes a Gaussian distribution of nanomagnet sizes based on SEM image analysis, the linewidth enhancement is predictable. The predicted linewidths from Ref. 8 are included in Fig. 7 as the dashed black line for the center mode and the blue line for the end mode. From the comparison of the predicted linewidths with the data, it is clear that size distribution alone does not fully account for the linewidth discrepancy between the end and center modes.

As an alternative to Eq. (3), we propose the following model to capture the essential physics associated with a process whereby a statistical distribution of asymmetric distortions in nanomagnet shape can lead to the broadening of the end-mode linewidth, as observed in Ref. 8. We assume a Gaussian distribution for the eggcentricity parameter c with zero mean, which results in a probability distribution of frequency splitting with a standard deviation σ_{ec}^f. Assuming the frequency distribution is not affected by the mode

frequency (equivalent to the assumption that the mode spatial profile is unaffected by the applied field), this distribution results in additional linewidth broadening with FWHM linewidth Δf_{ec}:

$$\Delta f_{ec} = 2(2 \ln 2)^{1/2} \sigma_{ec}^f. \tag{4}$$

The frequency linewidth Δf_{ec} due to the distribution of eggcentricity can be converted into a field swept linewidth $\mu_0 \Delta H_{ec}(H)$ according to

$$\mu_0 \Delta H_{ec}(H) = \frac{\mu_0 \Delta f_{ec}}{\left(\frac{\partial f_0(H)}{\partial H}\right)} = \frac{\mu_0 2(2 \ln 2)^{1/2} \sigma_{ec}^f}{\left(\frac{\partial f_0(H)}{\partial H}\right)}, \tag{5}$$

where

$$f_0(H) = \frac{|\gamma| \mu_0}{2\pi} \sqrt{H \cdot (H + M_s)} \tag{6}$$

is the Kittel equation for this in-plane geometry.[20] Thus the conversion from the frequency linewidth Δf_{ec} to the field swept line $\mu_0 \Delta H_{ec}$ introduces a dependence of the inhomogenous linewidth broadening on the resonance field and therefore implicitly on the frequency. The total linewidth for the end mode can be then expressed in the following form:

$$\Delta H(f) = \Delta H_0 + \frac{4\pi\alpha}{|\gamma| \mu_0} \cdot f + \Delta H_{size}(f) + \Delta H_{ec}(f). \tag{7}$$

The first two terms are identical with the phenomenological Eq. (3), the third term $\Delta H_{size}(f)$ is the inhomogenous broadening caused by the size variation and the last term is the contribution due to the shape distortion of the nanomagnet.
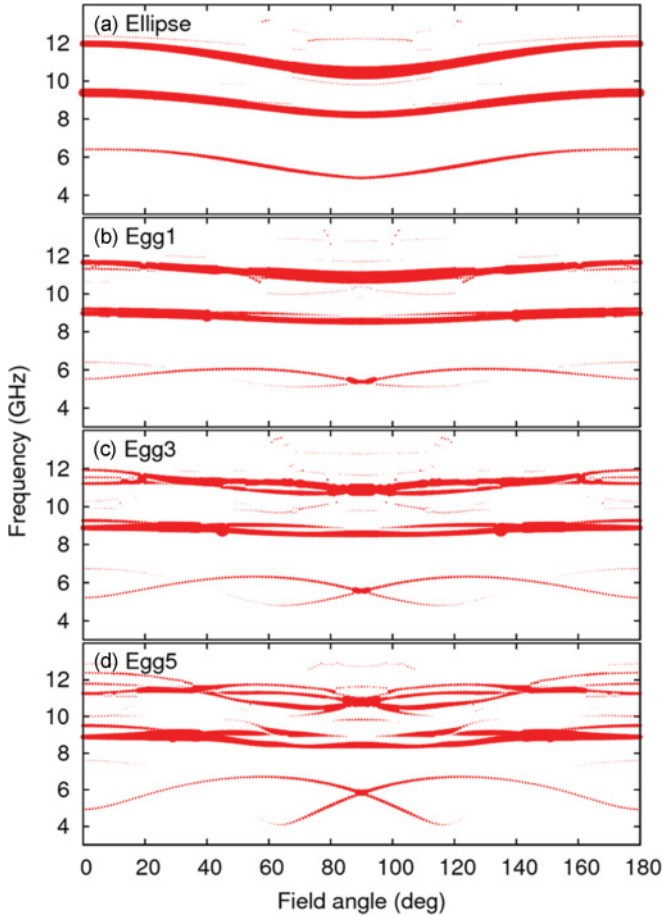
FIG. 6. (Color online) Angular dependence of the spin-wave modes determined by micromagnetic simulations. The thickness of the lines is proportional to the amplitude of the respective spin-wave mode.

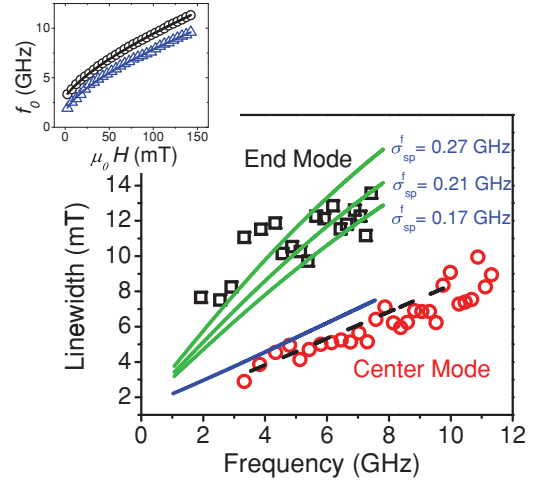

FIG. 7. (Color online) The frequency dependence of the FWHM linewidth for the center and the end modes measured by FR-MOKE in Ref. 8 for 5-nm-thick $Ni_{80}Fe_{20}$ 220 nm $\times$ 202 nm with the magnetic field applied parallel to the long axis of the ellipsoid. The dashed black and solid blue lines are calculated linewidths for the center and the end mode, respectively, where inhomogeneous broadening due to size variations alone are assumed. The green lines are predicted linewidths using a model where asymmetric shape distortions of egglike character are included in the model; see Eq. (7). The inset shows the resonance frequency versus applied field for the end mode (blue triangles) and the center mode (black circles).

For a Gaussian distribution of the size variations $\Delta H_{size}(f)$ is given by

$$\Delta H_{size}(f) = 2(2 \ln 2)^{1/2} \sigma_H(f), \qquad (8)$$

where $\sigma_H(f)$ is the distribution of the resonant field. See Ref. 8 for more details about the influence of the size distributions on the linewidth measured in an array of nanomagnets. The center mode is relatively unaffected by slight shape distortions, as verified in the BLS measurements. Thus the effect of the eggcentricity distribution on the center mode will be ignored. The green lines in Fig. 7 show the FWHM linewidth, which was calculated with Eq.(7) for standard deviations of $\sigma_{ec}^{f} = 0.17$, 0.21, and 0.27 GHz (labeled in the figure) in addition to the previously calculated contribution from experimentally determined size variations. We used a damping parameter value of $\alpha = 0.01$, as was previously measured in Ref. 8 for an unpatterned thin film of Permalloy. The range of values for σ_{ec}^{f} is still smaller than the $\sim$1-GHz splitting of the end mode observed in the egg3 sample for $\varphi = 0$. To within the signal-to-noise ratio of the linewidth data, the model provides a reasonable explanation for the measured linewidths. Moreover, the distribution in c increases the slope of the calculated linewidth, in qualitative agreement with the experimental data.

Thus a fit to the data with Eq. (3) would give rise to an apparent increase in α though the change in the slope is due to the distribution of the shape of the nanomagnets.

In a real array of nanomagnets, any asymmetric shape distortion is most likely not egglike. It is therefore expected that the model does not perfectly fit the data in Ref. 8. However, a mechanism of stochastic asymmetric shape distortions provides a plausible explanation for the data. Such distortions have a nontrivial effect on the mode frequencies, and, more importantly, differ in the degree of the effect, depending on the where the amplitude of precession is concentrated.

IV. SUMMARY

We investigated the influence of asymmetric shape distortions of a particular egglike character on the eigenmode spectra of magnetic nanostrucrures. BLS measurements reveal how shape distortions lift the frequency degeneracy of certain eigenmodes. This result was confirmed by micromagnetic simulations, which also clarified that the modes with the greatest eigenmode splittings are spatially concentrated at the ends of the nanomagnet. We then used this result to explain a previously reported measurement result, where it was found that the end mode in elliptical nanomagnets exhibits significantly larger linewidths than the center mode. We demonstrated here that a stochastic distribution of moderate asymmetric egg like shape distortions in an array of nominally identical nanomagnets leads to an increase in linewidth for the end mode at a scale comparable to that which was measured. On the other hand, we also find that the center-mode

linewidth was minimally affected by such random variations in nanomagnet shape, in agreement with both our expectations based upon elementary reasoning of how demagnetizing fields affect the mode frequency, as well as previously reported data in Ref. 8.

[1] L. Berger, Phys. Rev. B **54**, 9353 (1996).

[2] J. C. Slonczewski, J. Magn. Magn. Mater. **159**, L1 (1996).

[3] H. T. Nembach, H. Bauer, J. M. Shaw, M. L. Schneider, and T. J. Silva, Appl. Phys. Lett. **95**, 062506 (2009).

[4] O. Klein, G. de Loubens, V.V. Naletov, F. Boust, T. Guillet, H. Hurdequint, A. Leksikov, A.N. Slavin, V.S. Tiberkevich, and N. Vukadinovic, Phys. Rev. B **78**, 144410 (2008).

[5] J. C. Sankey, P.M. Braganca, A.G.F. Garcia, I.N. Krivorotov, R.A. Buhrman, and D.C. Ralph, Phys. Rev. Lett. **96**, 227601 (2006).

[6] N.C. Emley, I.N. Krivorotov, O. Ozatay, A.G.F. Garcia, J.C. Sankey, D.C. Ralph, and R.A. Buhrman, Phys. Rev. Lett. **96**, 247204 (2006).

[7] M. L. Schneider, J.M. Shaw, A.B. Kos, Th. Gerrits, T.J. Silva, and R.D. McMichael, J. Appl. Phys. **102**, 103909 (2007).

[8] J.M. Shaw, T. J. Silva, M. L. Schneider, and R.D. McMichael, Phys. Rev. B **79**, 184404 (2009).

[9] P. S. Keatley, V.V. Kruglyak, A. Neudert, E.A. Galaktionov, R.J. Hicken, J.R. Childress, and J.A. Katine, Phys, Rev. B **78**, 214412 (2008).

[10] V. E. Demidov, M. Buchmeier, K. Rott, P. Krzysteczko, J. Munchenberger, G. Reiss, and S.O. Demokritov, Phys. Rev. Lett. **104**, 217203 (2010).

[11] J.R. Sandercock, Solid State Commun. **15**, 1715 (1974).

[12] G. Gubbiotti, G. Carlotti, T. Okuno, M. Grimsditch, L. Giovannini, F. Montoncello, and F. Nizzoli, Phys. Rev. B **72**, 184419 (2005).

[13] J. Jorzick, S.O. Demokritov, C. Mathieu, B. Hillebrands, B. Bartenlian, C. Chappert, F. Rousseaux, and A.N. Slavin, Phys. Rev. B **60**, 15194 (1999).

[14] G. Gubbiotti, G. Carlotti, T. Okuno, M. Grimsditch, L. Giovannini, F. Montoncello, and F. Nizzoli, J. Appl. Phys. **99**, 08C701 (2006).

[15] M. Buchmeier, H. Dassow, D.E. Burgler, and C.M. Schneider, Phys. Rev. B **75**, 184436 (2007).

[16] M.J. Donahue and D.G. Porter, Internal Report No. NISTIR 6376, Natl. Inst. Stand. Technol., 1999.

[17] J.M. Vaughan, *The Fabry-Perot Interferometer* (Taylor and Francis, New York, 1989).

[18] R.D. McMichael and M.D. Stiles, J. Appl. Phys. **97**, 10J901 (2005).

[19] Th. D. Rossing, J. Appl. Phys. **34**, 995 (1963).

[20] Ch. Kittel, Phys. Rev. **73**, 155 (1948).